The Astronomical Journal, 166:41 (14pp), 2023 August https://doi.org/10.3847/1538-3881/acdb75

A Spectroscopic Thermometer: Individual Vibrational Band Spectroscopy with the Example of OH in the Atmosphere of WASP-33b

Sam O. M. Wright[1], Stevanus K. Nugroho[2,3], Matteo Brogi[4,5,6], Neale P. Gibson[7], Ernst J. W. de Mooij[8], Ingo Waldmann[1], Jonathan Tennyson[1], Hajime Kawahara[9], Masayuki Kuzuhara[2,3], Teruyuki Hirano[2,3,10], Takayuki Kotani[2,3,10], Yui Kawashima[11], Kento Masuda[12], Jayne L. Birkby[13], Chris A. Watson[14], Motohide Tamura[2,3,15], Konstanze Zwintz[16], Hiroki Harakawa[17], Tomoyuki Kudo[17], Klaus Hodapp[18], Shane Jacobson[18], Mihoko Konishi[19], Takashi Kurokawa[3,20], Jun Nishikawa[2,3,10], Masashi Omiya[2,3], Takuma Serizawa[3,20], Akitoshi Ueda[2,3,10], Sébastien Vievard[2,17], and Sergei N. Yurchenko[1]
[1] Department of Physics and Astronomy, University College London, Gower Street, WC1E 6BT, London, UK; swright@star.ucl.ac.uk
[2] Astrobiology Center, NINS, 2-21-1 Osawa, Mitaka, Tokyo 181-8588, Japan
[3] National Astronomical Observatory of Japan, NINS, 2-21-1 Osawa, Mitaka, Tokyo 181-8588, Japan
[4] Dipartimento di Fisica, Università degli Studi di Torino, via Pietro Giuria 1, I-10125, Torino, Italy
[5] Department of Physics, University of Warwick, Coventry, CV4 7AL, UK
[6] INAF-Osservatorio Astrofisico di Torino, Via Osservatorio 20, I-10025 Pino Torinese, Italy
[7] School of Physics, Trinity College Dublin, The University of Dublin, Dublin 2, Ireland
[8] Astrophysics Research Centre, Queen's University Belfast, Belfast, BT7 1NN, UK
[9] Department of of Space Astronomy and Astrophysics, Institute of Space and Astronautical Science, Japan Aerospace Exploration Agency, 3-1-1, Yoshinodai, Chuo-ku, Sagamihara, Kanagawa 252-5210, Japan
[10] Department of Astronomy, School of Science, The Graduate University for Advanced Studies (SOKENDAI), 2-21-1 Osawa, Mitaka, Tokyo 181-8588, Japan
[11] Cluster for Pioneering Research, RIKEN, 2-1 Hirosawa, Wako, Saitama 351-0198, Japan
[12] Department of Earth and Space Science, Osaka University, Osaka 560-0043, Japan
[13] Astrophysics, Department of Physics, University of Oxford, Keble Road, Oxford, OX1 3RH, UK
[14] School of Mathematics and Physics, Queen's University Belfast, University Road, Belfast, BT7 1NN, UK
[15] Department of Astronomy, Graduate School of Science, The University of Tokyo, 7-3-1 Hongo, Bunkyo-ku, Tokyo 113-0033, Japan
[16] Institute for Astro- and Particle Physics, University of Innsbruck, Technikerstrasse 25/8, A-6020 Innsbruck, Austria
[17] Subaru Telescope, 650 N. Aohoku Place, Hilo, HI 96720, USA
[18] University of Hawaii, Institute for Astronomy, 640 N. Aohoku Place, Hilo, HI 96720, USA
[19] Faculty of Science and Technology, Oita University, 700 Dannoharu, Oita 870-1192, Japan
[20] Institute of Engineering, Tokyo University of Agriculture and Technology, 2-24-16, Nakacho, Koganei, Tokyo 184-8588, Japan
Received 2023 February 2; revised 2023 May 18; accepted 2023 June 1; published 2023 July 4

Abstract

Individual vibrational band spectroscopy presents an opportunity to examine exoplanet atmospheres in detail, by distinguishing where the vibrational state populations of molecules differ from the current assumption of a Boltzmann distribution. Here, retrieving vibrational bands of OH in exoplanet atmospheres is explored using the hot Jupiter WASP-33b as an example. We simulate low-resolution spectroscopic data for observations with the JWST's NIRSpec instrument and use high-resolution observational data obtained from the Subaru InfraRed Doppler instrument (IRD). Vibrational band–specific OH cross-section sets are constructed and used in retrievals on the (simulated) low- and (real) high-resolution data. Low-resolution observations are simulated for two WASP-33b emission scenarios: under the assumption of local thermal equilibrium (LTE) and with a toy non-LTE model for vibrational excitation of selected bands. We show that mixing ratios for individual bands can be retrieved with sufficient precision to allow the vibrational population distributions of the forward models to be reconstructed. A fit for the Boltzmann distribution in the LTE case shows that the vibrational temperature is recoverable in this manner. For high-resolution, cross-correlation applications, we apply the individual vibrational band analysis to an IRD spectrum of WASP-33b, applying an "unpeeling" technique. Individual detection significances for the two strongest bands are shown to be in line with Boltzmann-distributed vibrational state populations, consistent with the effective temperature of the WASP-33b atmosphere reported previously. We show the viability of this approach for analyzing the individual vibrational state populations behind observed and simulated spectra, including reconstructing state population distributions.

Unified Astronomy Thesaurus concepts: Astronomy data modeling (1859); Exoplanet atmospheres (487); Exoplanet atmospheric composition (2021); Hot Jupiters (753); High resolution spectroscopy (2096); Near infrared astronomy (1093)

1. Introduction

The study of exoplanet atmospheres is motivated by a desire to understand the physical properties of exoplanets and their origins. These properties reflect a range of planetary environments that can differ drastically from those in our solar system and are yet to be fully understood; to gain a better understanding, we must determine their atmospheric composition and thermal structure. We can also extract valuable information about the origins of these planets and their formation histories, including information about planetary migration and constraints on the modeling of protoplanetary disks (Öberg et al. 2011). Beyond enhancing our current

understanding, characterizing exoplanets can inform the direction of future research, targets for follow-up study, and the priorities for designing future space missions and ground-based facilities.

We deduce these characteristics via the process of retrieval; this allows us to infer parameters related to the atmosphere's composition and structure from spectroscopic data acquired by observing the planet. Spectra are produced based on atmospheric models of the physical processes taking place and the radiative transfer of photons through the planet's atmosphere. Statistical techniques (typically Bayesian inference methods) are used to match the modeled spectra with the observed spectral data, given models produced with the chosen parameterization. Optimal values for the parameters are found via these methods, where optimal is quantified as the maximum a posteriori probability.

Typically, the temperature profiles in exoplanetary atmospheric retrievals are obtained via the fitting of a complex atmospheric model to an observed absorption (transit) or emission spectrum, where the temperature is one of the factors shaping the spectral profile. Most notably, temperature affects the magnitude (intensity) of different absorption/emission bands as well as their shapes (e.g., Tessenyi et al. 2013). Here we explore an alternative, "spectroscopic thermometer" approach, based on the relative intensities of individual molecular bands as an estimate of their vibrational populations and therefore the corresponding vibrational temperature. Knowledge of vibrational state populations obtained via band-by-band retrievals provides an opportunity to infer the molecular vibrational temperature directly from their spectral features. Additionally, any outlying band population would indicate the molecule's departure from the local thermal equilibrium (LTE) within the planet's atmosphere. Especially favorable for this purpose are the (hot) bands of some molecules, which are characterized by substantial displacement from each other within a relatively small spectroscopic region (Wright et al. 2022); typical examples are diatomics and linear polyatomics. The ability to analyze molecular spectra with such granularity will play an increasingly important role in the characterization of exoplanet atmospheres, as accounting for divergences from local thermodynamic equilibrium could greatly impact our understanding of atmospheric conditions, such as temperature structure (Fisher & Heng 2019; Fossati et al. 2021) and wind characteristics (Borsa et al. 2021).

While the approach outlined here naturally enables non-LTE analyses, it also provides advantages for LTE atmospheric analysis with high- and low-resolution observations. For high-resolution data, it allows temperature measurement without needing to run computationally expensive temperature–pressure (T-P) profile retrievals. When analyzing low-resolution data, this approach can serve as a separate temperature diagnostic tool with the potential to avoid degeneracies in temperature retrieval results.

Here we consider the hydroxyl radical (OH) in the atmosphere of WASP-33b both for low-resolution and high-resolution applications. OH has recently been detected in the atmosphere of WASP-33b using the cross-correlation technique (Nugroho et al. 2021a), with data from the Subaru telescope's InfraRed Doppler instrument (IRD; $R \approx 70{,}000$; Tamura et al. 2012; Kotani et al. 2018) in the spectral region of 0.97–1.75 μm, which was later confirmed by Cont et al. (2022) using CARMENES data. This near-infrared (NIR) region contains the OH emission bands formed by the $\Delta v = 2$ rotation-vibrational transitions from vibrational states populated at the relevant temperature of the atmosphere. The OH spectrum has good wavelength separation between hot vibrational bands. In this work, we aim to use this feature to disentangle individual band intensities in the atmospheric retrievals in order to target their individual vibrational populations, i.e., to use information beyond the aggregated band-level information found in the molecular data typically employed for exoplanet atmospheric analyses. We will show that the separation between the OH bands in the NIR is sufficient for the bands to be individually retrievable, even with the current observation technology, despite the usual degeneracy of the atmospheric factors in a typical retrieval of the atmospheres of hot Jupiters. While spectral signatures have been shown to differ in non-LTE for other molecules (Wright et al. 2022), it is also worth investigating OH, in particular when considering non-LTE in exoplanet atmospheres, since it has a well-documented airglow effect in Earth's atmosphere (Meinel 1950; Noll et al. 2020) and the Martian atmosphere (Clancy et al. 2013). In non-LTE circumstances, vibrational state populations diverge substantially from a Boltzmann distribution (as shown in Chen et al. 2021), which makes the selection of OH particularly relevant for this analysis.

2. NIR Spectrum of OH and Cross-section Generation

Our goal is to investigate the possibility of retrieving individual vibrational populations of OH in the NIR emission spectrum of a hot Jupiter–like atmosphere, using WASP-33b as an example. The MoLLIST line list (Brooke et al. 2016) for OH is used, along with the ExoCross software (Yurchenko et al. 2018) for molecular cross-section generation. The software provides two capabilities crucial to this investigation: the means to filter individual vibrational bands (i.e., to select isolated bands, while still assuming a Boltzmann distribution under the LTE condition) and also to supply custom state populations from which cross sections can be calculated.

The NIR spectrum of OH is mainly composed of the $\Delta v = 2$ vibrational bands, including the overtone band (2, 0), as well as the weaker $\Delta v = 3$ bands; see Figure 2, where an LTE spectrum of OH for the equilibrium temperature of $T = 3050$ K is shown, with the individual bands ($\Delta v = 2$ and $\Delta v = 3$) depicted in different colors. Here, assuming the LTE conditions, cross sections of seven (in the first instance) individual vibrational bands ($0 \leqslant v'' \leqslant 6$) of OH were generated using a grid spacing of 0.03 cm^{-1}; this grid spacing corresponds to a minimum resolving power of $R \approx 190{,}000$ (at 1.75 μm), which allowed us to retain flexibility at the modeling stage and the potential for applications of the cross section set to higher-resolution data in the future. The constant grid spacing allows us to guarantee that we did not introduce artifacts from the grid subdivision performed by ExoCross to achieve a fixed resolution across the wavelength range. The vibrational bands were individually isolated via the filtration method, where ExoCross selects only those spectroscopic lines originating from the desired vibrational state. In line with the LTE approximation, their magnitudes drop due to the Boltzmann factor as well as the corresponding vibrational band strength. For reference, we also retained the standard set of cumulative cross sections of OH for modeling the contribution of OH in LTE to the spectrum of WASP-33b. Although our goal is to examine the effects in emission, we remain consistent with

atmospheric codes by generating cross sections for the absorption case. Atmospheric modeling codes (such as TauREx 3; Al-Refaie et al. 2021) ingest absorption data and model the emission case using these absorption data equivalently by Kirchoff's law under the assumption of LTE.

In order to be able to retrieve populations of individual bands of OH in atmospheric spectroscopic models, individual band cross sections were generated with normalized populations (the state population being set to 1) as a sum of all line intensities for transitions $f \leftarrow i$ from a given vibrational band (v', v'') (Yurchenko et al. 2018):

$$\sigma(\tilde{\nu})_{v',v''} = \sum_{i,f} f_{if}(\tilde{\nu}) \frac{A_{if}^{(v',v'')} N_{\mathrm{r-v}}}{8\pi c^2 \tilde{\nu}_{if}^2} (1 - e^{-hc\tilde{\nu}_{if}/kT}), \quad (1)$$

where $f_{if}(\tilde{\nu})$ is a line profile, $A_{if}^{(v',v'')}$ is the corresponding Einstein A coefficient, and $N_{\mathrm{r-v}}$ is a population of the lower rotation-vibration state (v'', i).

In order to separate the vibrational and rotational populations in our analysis, we use the following approximation of a product of these contributions:

$$N_{\mathrm{r-v}} = N_v N_{\mathrm{rot}}, \quad (2)$$

where N_v is a population of the vibrational (or vibronic) state v and N_{rot} is the population of the rotational state. For the rotational population, a Boltzmann distribution is assumed, with the rotational temperature T_{rot}—the same as the structural temperature of the atmosphere, as defined by the atmospheric T-P profile—taken for calculating the scale height. This approximation is similar to the Treanor distribution, where the rotational and vibrational components are separated, as discussed in Treanor et al. (1968). The Treanor distribution takes the product of two Boltzmann distributions: one in terms of the rotational temperature and one in terms of the vibrational temperature. We make this assumption for the temperature in Equation (1) such that $T = T_{\mathrm{rot}}$. The effect of the vibrational population is to scale each of the band intensities by the population of the state v. For example, the vibrational Boltzmann population is obtained using the formula

$$N_v = \frac{e^{-E_v/kT_{\mathrm{vib}}}}{Q_v(T)}, \quad (3)$$

where E_v is the vibrational energy of the state, $Q_v(T)$ is the temperature-dependent vibrational partition function, and k is the Boltzmann constant. We can relate this back to Figure 2, which shows this for the circumstance where $T_{\mathrm{vib}} = T_{\mathrm{rot}}$, i.e., under the LTE condition. In this work, we aim to retrieve the populations N_v directly from the exoplanetary spectrum as an independent measure of the atmospheric temperature via T_{vib}.

At this step, we use ExoCross to generate cross sections for OH with bespoke populations $N_{\mathrm{r-v}}$ for each of the states defined in the MoLLIST OH line list. The ExoCross software applies these populations for each state with the corresponding vibrational quantum number. Individual vibrational populations can be provided in the ExoCross program in order to isolate each desired band; in each case, the vibrational population N_v was set to 1 for the desired state and 0 for the remaining states, and a partition function is inferred. Using this method, we produced seven sets of cross sections for each of the lower states ($v'' = 0$, 1, 2, 3, 4, 5, and 6) of the hydroxyl radical for the $\Delta v = 2$ and $\Delta v = 3$ bands; i.e., those where opacity falls into the NIR window <1.8 μm. The corresponding population of each band was normalized to 1 for temperatures ranging between 2850 K and 3350 K and pressures between 1×10^{-8} bar and 100 bar, which covers the T-P profile of WASP-33b, which follows a Guillot (2010) profile, as shown in Figure 1. The resulting cross sections are plotted in Figure 3 for a rotational temperature of $T_{\mathrm{rot}} = 3050$ K and $N_v = 1.0$, where individual spectral components of the hydroxyl radical are shown; all the bands are overlaid in the top pane to show their relative intensities and then plotted individually below for clarity.

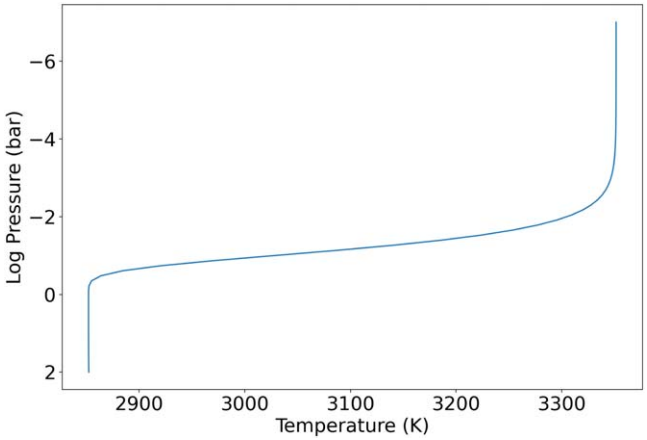

Figure 1. The Guillot T-P profile adopted for modeling the atmosphere of WASP-33b.

Bands with different lower-state excitations $v'' \leqslant 5$ are indicated by different colors. The stronger features on the right are from the $\Delta v = 2$ bands, while the weaker features on the left are from the $\Delta v = 3$ bands. The labels $v0$, $v1$, $v2$, … indicate the lower vibrational states 0, 1, 2, …, respectively.

For this case, we see that the strengths of the $\Delta v = 2$ bands increase with v quadratically, using an extension of the double harmonic approximation to the overtone bands (Clark & Yurchenko 2021), while the intensity increase of the $\Delta v = 3$ band is approximately cubic (Pastorek et al. 2022). Due to the relative line strengths, the $\Delta v = 3$ sequence will be far less significant than the $\Delta v = 2$ band features, until the $v5$ ($v'' = 5$) and $v6$ ($v'' = 6$) systems. The weaker $\Delta v = 3$ bands are also included as being present within our chosen spectral range. As $\Delta v = 2$ moves away from the window, for $v'' > 4$, only $\Delta v = 3$ bands remain visible.

To come full circle for the sake of illustration, the original LTE spectrum at a given T can then be reconstructed from these $N_v = 1$ vibrational band isolated cross sections, by scaling the individual band cross sections for given $T = T_{\mathrm{rot}}$ to the actual population number N_v in Equation (3). For example, the cross sections in Figure 2 were obtained by scaling the cross sections from Figure 3 using N_v from Equation (3). Accordingly, there is an additional drop in their intensities with increasing v.

3. Forward Modeling

Forward modeling of the emission spectrum of WASP-33b was performed by taking the requisite input parameters from Nugroho et al. (2021a), listed in Table 1. These planetary and stellar parameters were used along with the generated cross sections and the atmospheric modeling code TauREx 3

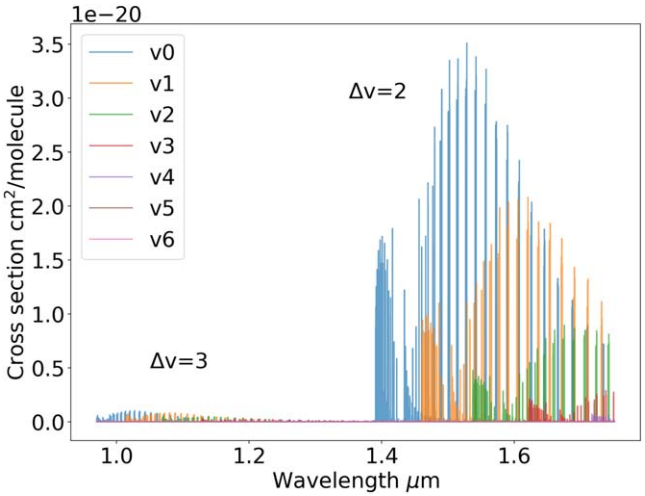

Figure 2. Individual band contributions for cross sections of OH in LTE, with the NIR ($\Delta v = 2$ and $\Delta v = 3$) bands shown for the 3050 K, 0.01 bar point on the T-P grid.

(Al-Refaie et al. 2021) to produce atmospheric models. The standard, unfiltered cross sections were used to generate a forward model of OH in WASP-33b's atmosphere, as shown in Figure 4; this was performed with the raw OH cross sections, allowing the retention of the native high-resolution models for high-resolution cross-correlation analysis and the later down-binning during the observation simulations for the low-resolution space-borne analysis.

4. James Webb Observation Simulations and Retrievals

4.1. Observation Simulations

Simulations of observations of WASP-33b's atmosphere with JWST using the G140H configuration of the NIRSpec instrument were conducted using ExoWebb (Edwards & Stotesbury 2021) noise simulation along with Pandeia data (Pontoppidan et al. 2016) incorporated into TauREx's instrument simulation code. The simulation is shown in Figure 4 for a ten-secondary-eclipse simulation of WASP-33b, overlaying the TauREx forward model for comparison. An increasing number of simulated secondary eclipses yielded simulated observations with successively decreasing noise in the relative flux values. The ten-secondary-eclipse simulation shows the visibility of OH lines clearly in the wavelength region above 1.4 μm.

4.2. Retrievals of Vibrational Populations

Atmospheric retrievals of the populations of individual bands were performed with TauREx using a new non-LTE plugin (S. Wright 2023, in preparation) on the simulated observation data, using cross sections constructed as detailed in Section 2. Nested sampling was performed to fit for the log of the mixing ratios for the cross sections included in each case (log (OHn), with uniform priors between -12 and -1) and also the planetary radius (R_p with uniform priors between 1.5 and 2 R_J). The fit for planetary radius is included, to ensure any degeneracies in fitting are visible. From this, a derived mean molecular weight (μ) is calculated and its distribution displayed

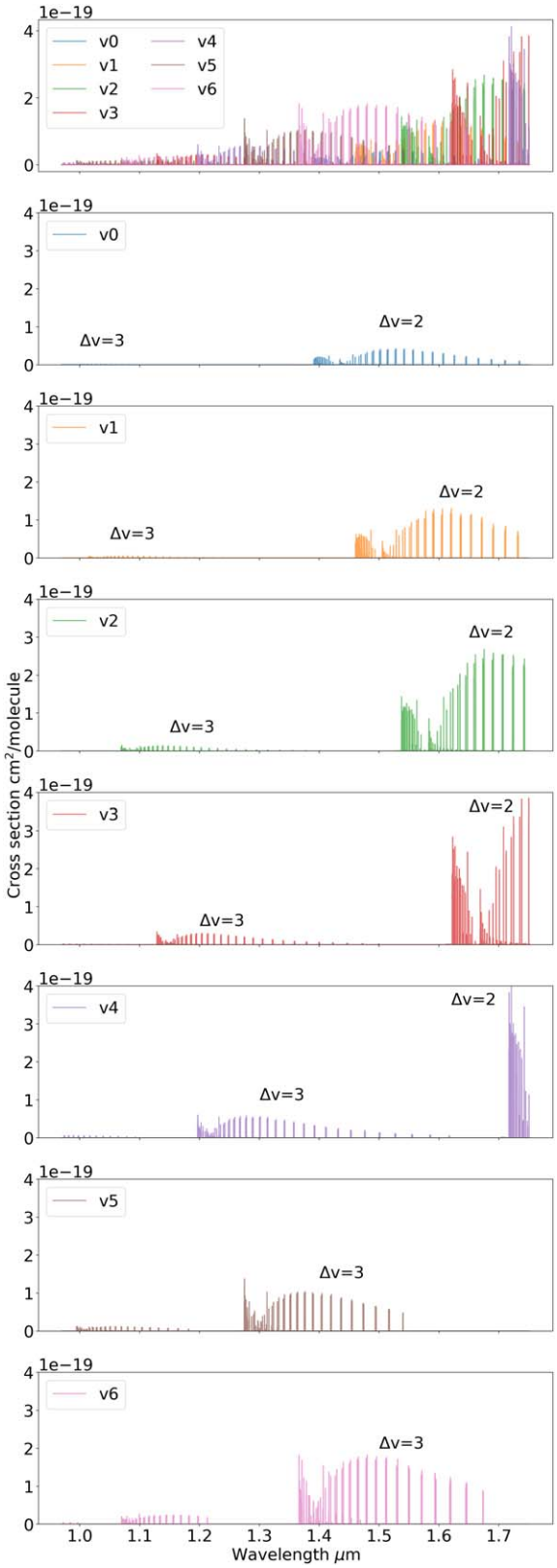

Figure 3. NIR cross sections of OH ($\Delta v = 2$ and $\Delta v = 3$) produced from the completely populated states plotted, overlaid in the top panel for scale and individually below, all at a temperature of 3050 K and a pressure of 0.01 bar. (Note that as we progress to the final two cross-section sets, the $\Delta v = 4$ and $\Delta v = 5$ bands start to become visible.)

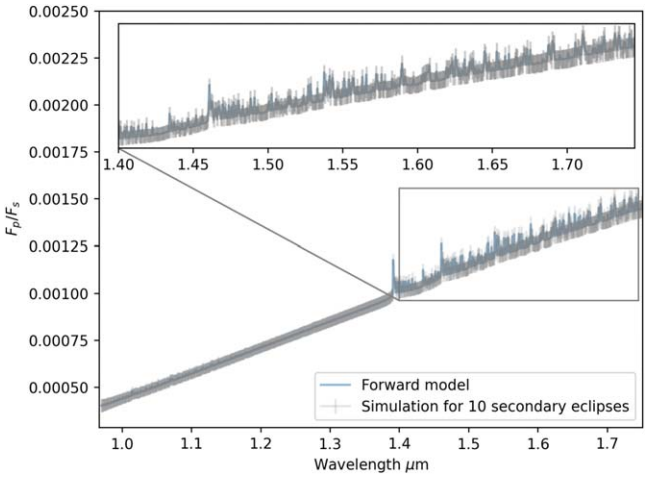

Figure 4. Observation simulation points and errors of the WASP-33b emission spectra plotted over the forward model for observations over ten secondary eclipses.

Table 1
Planetary and Stellar Parameters Used in Forward Modeling WASP-33b's Atmosphere

Parameter	WASP-33b Value
Planet Radius (R_J)	1.679
Planet Mass (M_J)	3.266
Stellar Temperature (K)	7400
Stellar Radius ($R_\odot$)	1.509
Stellar Metallicity (dex)	0.1
Semimajor Axis (au)	0.02558
Period (Days)	1.21987
OH Volume Mixing Ratio (VMR) Profile Parameters	
Surface VMR	7.94328×10^{-7}
Middle VMR	6.30957×10^{-5}
Top VMR	1×10^{-10}
Surface Pressure (Pa)	1×10^{7}
Middle Pressure (Pa)	3×10^{3}
Top Pressure (Pa)	1×10^{-3}

alongside the inferred probability distributions; this is included as a summary characteristic of the retrieved atmosphere.

The first set of retrievals was conducted using the cross sections corresponding to the vibrational Boltzmann LTE case as our baseline, where each band is effectively considered as an individual molecule, with the population predefined using the Boltzmann LTE rule in Equation (3), with $T_{\rm vib} = T_{\rm rot}$ following the T-P profile discussed in Section 2. This can be directly correlated with a population of an upper vibrational state v' or equivalently of a lower state v'', since we only deal with states differing by $\Delta v = 2$ or $\Delta v = 3$.

Based on this property, in the following, the vibrational bands in question, $v0$, $v1$, $v2$, etc., as labeled in Figure 3, will be referenced as bands 0, 1, 2, etc., i.e., using the corresponding lower-state v'' vibrational quantum number.

The mixing ratios for each band associated with v'' were considered in two ways: (i) following the three-point mixing profile used in the forward modeling step; and also (ii) using a constant mixing ratio. Though given the altitude of the thermal gradient modeled, the lower and upper points of the mixing profile cannot be well constrained on account of the limited pressure region probed by this wavelength; as such, we opted to proceed to perform retrievals with a constant mixing ratio profile.

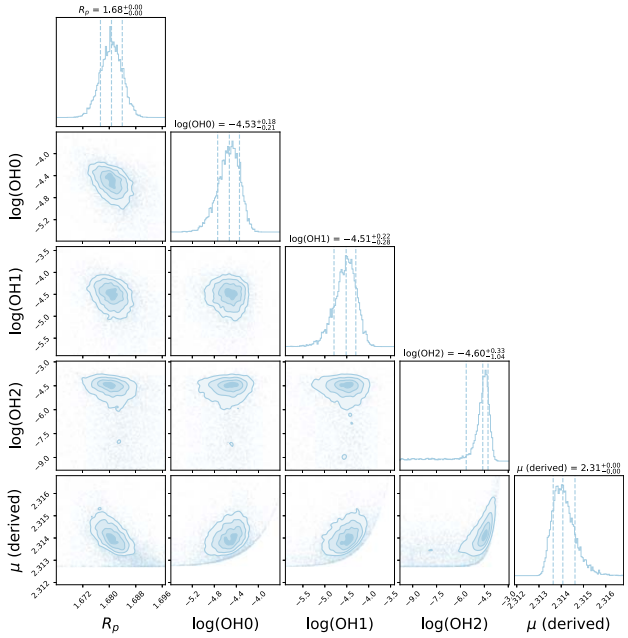

Figure 5. Retrieval nested sampling posteriors for one simulated secondary eclipse with bands 0–2.

Figure 5 shows the retrieved posterior probability distributions with the three strongest emission bands of OH in NIR, with $\Delta v = 2$ and $\Delta v = 3$, bands 0, 1, and 2 (i.e., corresponding to the emissions from the three states $v' = 2$, 3, and 4 with the highest populations). For this three-band case, treating each band as a separate species, a single secondary eclipse observation is sufficient to well constrain the individual band mixing ratios ($10^{-4.53}$, $10^{-4.51}$, and $10^{-4.60}$) to within reasonable agreement with the ground truth $10^{-4.2}$ (all within 2σ).

When we include the hotter band 3, the lines of which are weaker on account of the reduced relative populations, additional secondary eclipses are required to well constrain the band mixing ratios. The posteriors for a single secondary eclipse retrieval are shown in Figure 6, while the posteriors for retrievals conducted on five and ten secondary eclipses are shown in Figures 7 and 8, respectively. In this final retrieval, the band abundances are neatly constrained, with little degeneracy.

4.3. Spectroscopic Temperature Fitting from Vibrational Populations

We then attempted to deduce the temperature spectroscopically from the individual vibrational populations using the simulated data, again treating each emission band individually. We used the vibrational band cross sections with the population normalized to 1 ($N_v = 1$) introduced in Section 2. The retrieved mixing ratio now acts as a proxy for the band population (in addition to the information it contains about the overall mixing ratio of OH in the atmospheric model).

When considering the first three bands in isolation, using data simulated for five secondary eclipse observations, the mixing ratios for each of the individual bands can be well constrained (see Figure 9). The crucial difference compared to

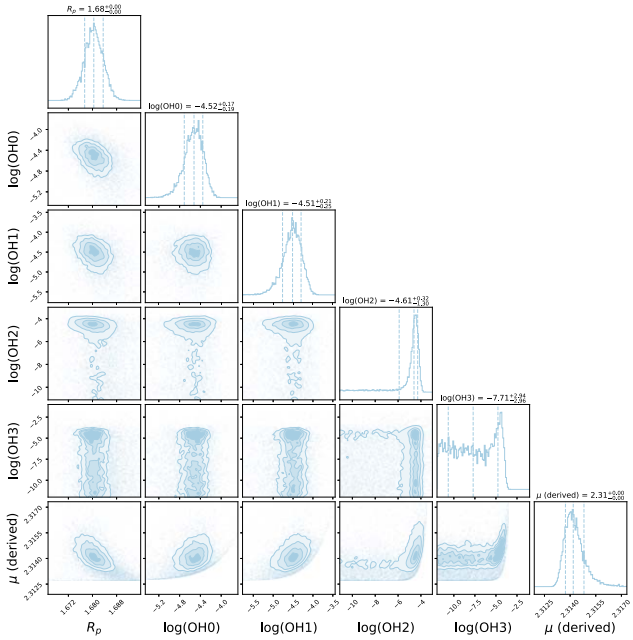

Figure 6. Retrieval nested sampling posteriors for one simulated secondary eclipse with bands 0–3.

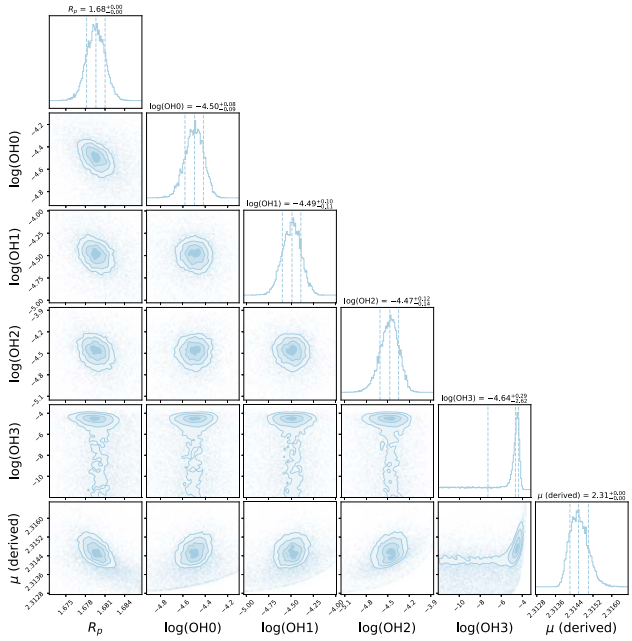

Figure 7. Retrieval nested sampling posteriors for five simulated secondary eclipses with bands 0–3.

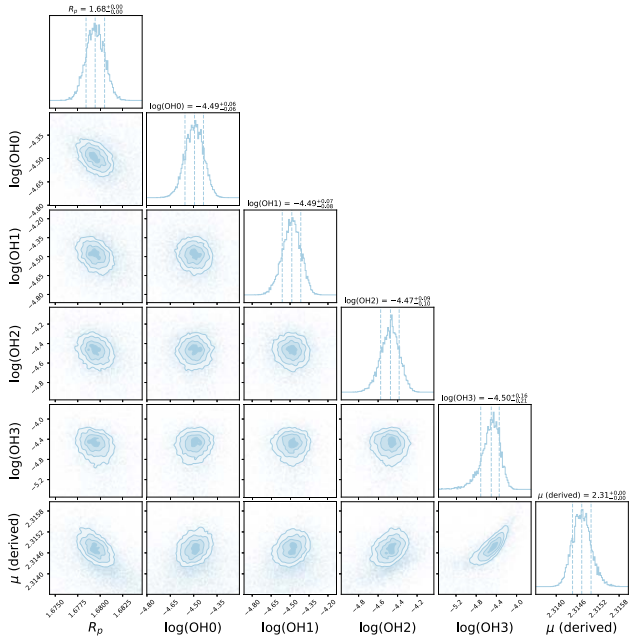

Figure 8. Retrieval nested sampling posteriors for ten simulated secondary eclipses with bands 0–3.

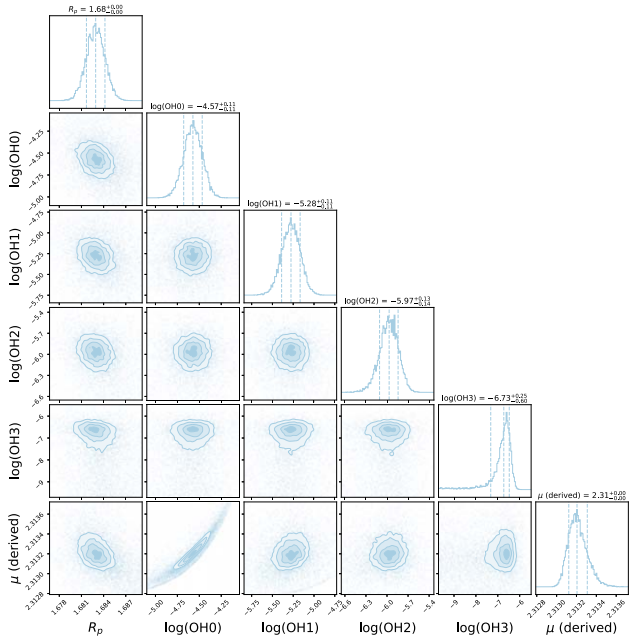

Figure 9. Posteriors for five simulated secondary eclipses with bands 0–3, using artificial completely populated band cross sections.

a typical retrieval of the mixing ratio for a molecule is that we see a drop off in the retrieved mixing ratio with increasing v'', corresponding to the reduced populations in higher bands for OH in LTE at this temperature. The relative weakness of the lines due to these higher states can be visualized in Figure 10, where the individual contributions used in the retrieval are plotted. The limit of our ability to retrieve such mixing ratios for less populated bands with ten simulated secondary eclipses of data is apparent in Figure 11 and is well understood by their marginal contribution to the OH spectra as well as by the limitations of the instrument.

In order to illustrate the limitations of detectability imposed by the low state populations and the associated limited emissions of very hot bands, in Figure 12 we examine the case of 50 secondary eclipse observations. One can see that even for this idealized case, only one more band can be constrained properly. For the subsequent two bands, only an upper limit can be given, and the 1σ confidence interval for the mixing ratio of these bands spans a wide, poorly constrained range, as shown in Figure 13.

We can now use this 50 simulated secondary eclipse retrieval to demonstrate the spectroscopic retrieval of the vibrational temperature $T_{\rm vib}$ via fitting the retrieved populations with a

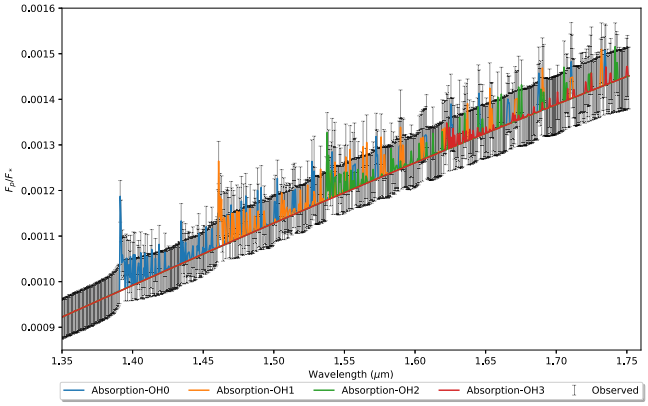

Figure 10. Individual band contributions of OH in NIR retrieved using the completely populated band cross sections for 0–3 with five simulated secondary eclipses, with the plot highlighting the wavelength region with the strongest lines.

Boltzmann distribution. The band mixing ratios retrieved individually using the individual complete band sets were normalized by their sum. We then employ a simple least squares fitting routine, with the vibrational temperature as our free parameter and the vibrational populations $N_v(T)$ given by Equation (3), from which we derive a best-fit vibrational temperature of 2815 K. It should be noted that this simulated example is not an independent measurement of the thermal conditions, since the literature T-P profile used in the simulation is assumed in the retrieval. Instead, it demonstrates the retrievability of vibrational populations as a technique, which could be used in conjunction with fitting the T-P profile when conducting such an analysis in the empirical case, with an unknown temperature profile.

The agreements between the Boltzmann distribution and the retrieved mixing ratios for the bands, as proxies for the band populations, are plotted in Figure 14. The bars show two population levels for each vibrational number, with the values given in Table 2; these arise since OH is an open-shell molecule and so fine-structure splitting gives rise to two energies per vibrational number.

4.4. Non-LTE Retrieval

In addition, we consider a hypothetical non-LTE scenario, where the vibrational state populations have been driven away from a Boltzmann distribution, similar to that shown for the excited bending vibrational mode of H_2O by Han et al. (2022). In our non-LTE scenario, we take the molecules to have been vibrationally excited to an arbitrary peak of $v = 3$, with the remaining state populations following a normal distribution around this peak, as shown in Table 2. This normally distributed configuration is an example of a non-Boltzmann population; the retrieval result is illustrated in Figure 15. An example of a physically occurring non-LTE scenario is the non-LTE vibrational population of OH in the airglow in the upper layers of the terrestrial atmosphere (Noll et al. 2020; Chen et al. 2021).

5. High-resolution Cross-correlation Approach

A high-resolution cross-correlation approach comprises part of this analysis. While we have demonstrated the theoretical capability to separate individual bands at the modeling stage and to integrate this into a retrieval framework, we were motivated by the limited resolution of such data from space-based observatories to investigate the use of high-resolution data from ground-based facilities. In this case, that is the IRD instrument on the Subaru telescope. To achieve this, we perform high-resolution cross-correlation fits for the free parameters: orbital velocity K_P, systemic velocity v_{sys}, and the scale factor of the model α. These fits are performed for a number of forward models, each of which has a fixed set of vibrational band contributions.

5.1. Observations and Data Reduction

We used three data sets taken after the secondary eclipse using the IRD mounted at the Subaru 8.2 m telescope. The first data set was obtained on 2020 October 1 (N1, PID: S20B-008, PI: Nugroho) and used to detect OH emission; see Nugroho et al. (2021a), while the additional two data sets were taken on 2021 August 30 (N2) and 2021 December 18 (N3) as part of program S21B-111 (PI: Nugroho; see Table 3 for the observation log). The target was continuously observed in natural guide star mode without the laser frequency comb, with an exposure time of 300 s per frame and overhead time of 25 s. We discarded the first nine exposures of N3, which had a low signal-to-noise ratio (S/N) due to high humidity. These data sets are part of the work of S. Nugroho et al. (2023, in preparation), and we refer the reader there for full details.

In short, the data were reduced using the IRD pipeline (Kuzuhara et al. 2018; M. Kuzuhara et al. 2023, in preparation). The extracted spectra consist of 72 spectral orders ranging from ≈9260 to ≈17645 Å. We exclude the first eight and the last spectral orders, due to relatively low S/N. In addition, we also exclude the spectral orders with a median wavelength between 14600 and 15203 Å from further analysis, due to heavy telluric contamination. We fit the continuum profile of the spectrum with the highest S/N of each data set, using the CONTINUUM task in IRAF.[21] Then we divided the data sets by their corresponding best-fit continuum profile to normalize them. The sky emission lines were masked, based on Oliva et al. (2015) and Rousselot et al. (2000). The spectra were put into a "common blaze function/continuum profile," following the procedure of Merritt et al. (2020). Any 5σ outliers were masked from the data, following Gibson et al. (2020). Any remaining bad pixels and bad regions were visually identified and masked out from the data. The final spectra of each data set were then stacked into an array with three axes: number of spectral orders (58), number of exposures, and wavelength (2048). Finally, we also masked the pixels that have a value less than 0.1 from the data, to avoid any saturated telluric lines, and estimated the uncertainty of each pixel by calculating the outer product of the standard deviation along the wavelength and time, then normalized by the standard deviation of the whole array excluding the masked pixels.

In the wavelength range of IRD, telluric and stellar lines dominate the data. The signal of the planet is several orders of magnitude weaker than the signal of the host star. To extract the planet signal using the cross-correlation technique pioneered by Snellen et al. (2010), the telluric and stellar lines must be removed from the data. Fortunately, the radial velocity of the planet ranged from tens to hundreds of kilometers per

[21] The Image Reduction and Analysis Facility (IRAF) is distributed by the US National Optical Astronomy Observatories, operated by the Association of Universities for Research in Astronomy, Inc., under a cooperative agreement with the National Science Foundation.

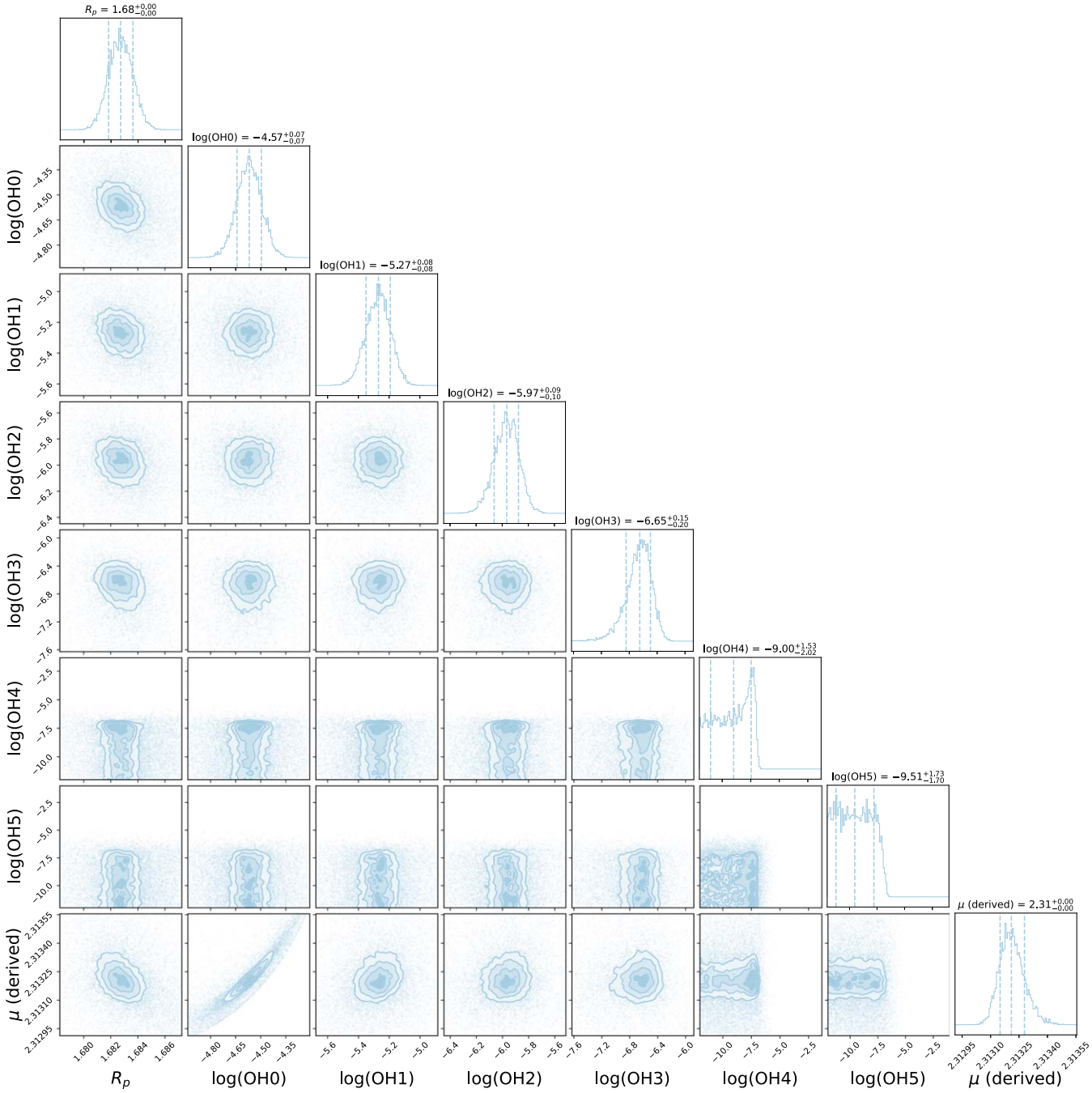

Figure 11. Posteriors for ten simulated secondary eclipses with bands 0–5, using artificial completely populated band cross sections.

second, shifting the planet spectra across many different pixels, while the telluric and stellar lines were (quasi-)stationary during the observations. To remove them, first, we divided out the mean spectra from each data set. We then applied the detrending algorithm SysRem (Tamuz et al. 2005) independently to each spectral order in each data set to remove the temporal variations in each wavelength bin. This was first applied to high-resolution data sets by Birkby et al. (2013). Any wavelength bin in the residual of each iteration of each spectral order that has a standard deviation of more than five times the standard deviation of the whole array was masked. We stopped the iteration when the detection strength of OH was at its maximum (see Table 3 for the number of iterations selected for each data set).

5.2. Cross-correlation and Likelihood Mapping

We cross-correlated the telluric-cleaned data sets with our forward models, Doppler-shifted using linear interpolation over a range of radial velocity. We used the cross-correlation function of Gibson et al. (2020):

$$\mathrm{CCF}(v) = \sum_i \frac{f_i m_i(v)}{\sigma_i^2}, \tag{4}$$

where CCF is the cross-correlation function for a given Doppler-shifted velocity (v), f_i is the mean-subtracted telluric-cleaned data at the ith wavelength bin, σ_i is the uncertainty, and m_i is the mean-subtracted model Doppler-shifted to a radial velocity of v.

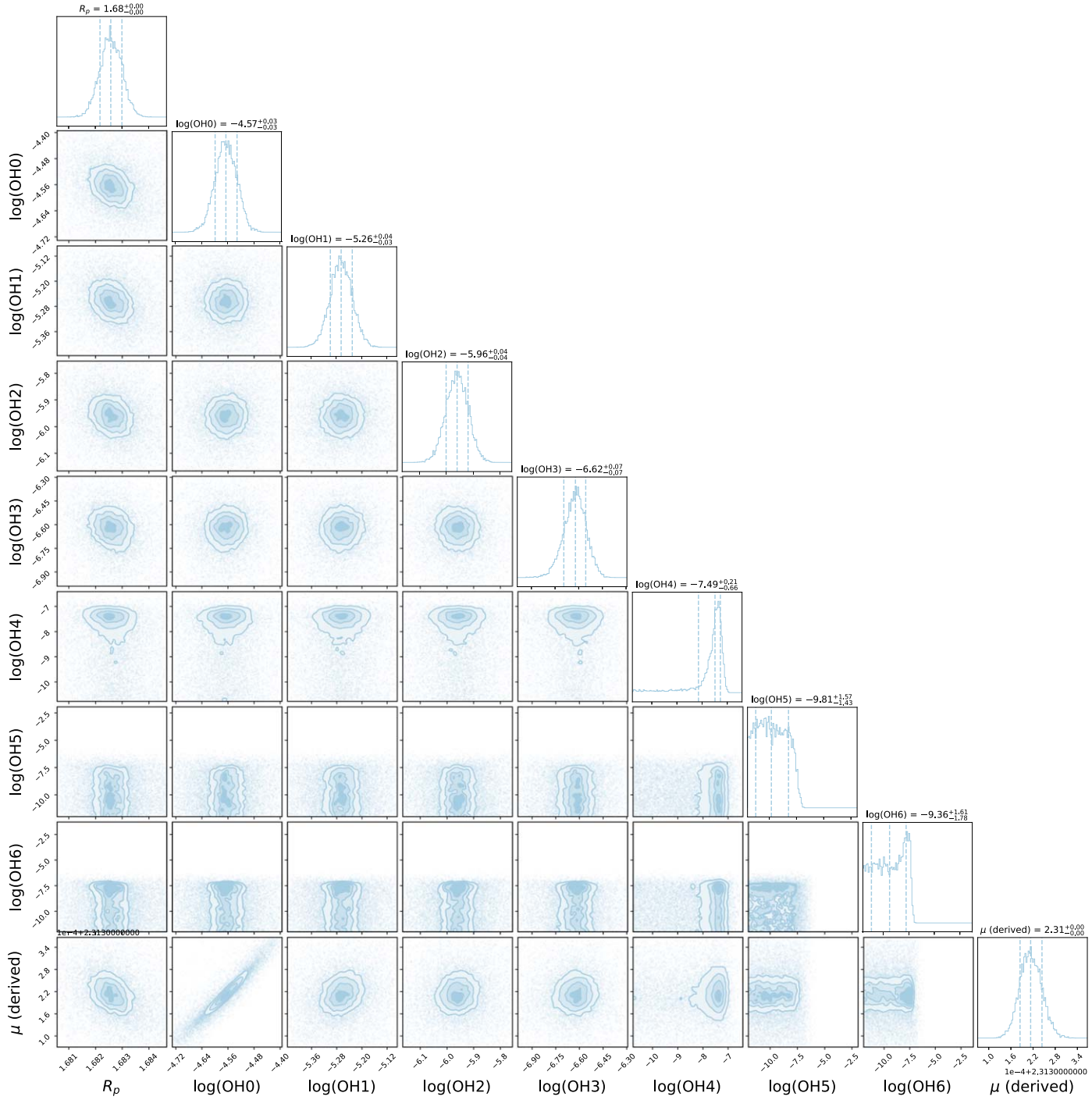

Figure 12. Posteriors for the retrieval including bands 0 through 6 for 50 simulated secondary eclipses.

The cross-correlation functions of all of the data sets were then coadded at the planetary rest frame over a range of orbital velocity (K_P) and systemic velocity (v_{sys}), creating a K_P–v_{sys} CCF map. We then converted it to an S/N map, by dividing it by the standard deviation of the area ± 50 km s^{-1} away from the expected signal. Based on previous studies, the planetary signal, if any, would appear around a K_P of 230 km s^{-1} and v_{sys} of -3 km s^{-1} (e.g., Nugroho et al. 2017, 2020, 2021b; Cont et al. 2021, 2022; Yan et al. 2021, 2022; van Sluijs et al. 2022).

To avoid any bias in selecting which area to represent the noise, we followed Brogi et al. (2023) by fitting a Gaussian function to the CCF distribution of the noise and using the best-fit standard deviation as the estimated noise floor.

We also calculated a likelihood map ($\mathcal{L}$) for each model using the β-optimized likelihood function, following Gibson et al. (2020; see also Brogi & Line 2019):

$$\ln \mathcal{L}(v) = -\frac{N}{2} \ln \left[\frac{1}{N} \left(\sum \frac{f_i^2}{\sigma_i^2} + \alpha^2 \sum \frac{m_i(v)^2}{\sigma_i^2} - 2\alpha \mathrm{CCF}(v) \right) \right], \quad (5)$$

where α is the scale factor of the model and N is the total number of pixels.

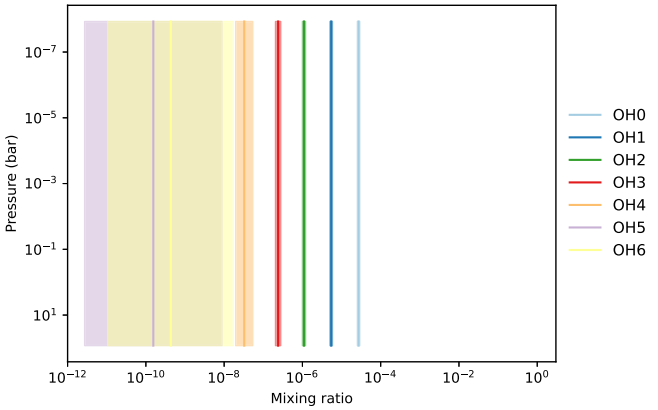

Figure 13. Mix ratios retrieved for bands 0 through 6 for 50 simulated secondary eclipses.

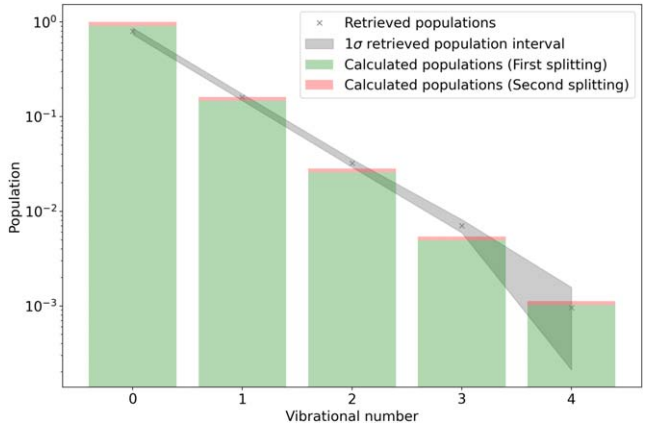

Figure 14. Retrieved mixing ratios for OH compared with the theoretical Boltzmann distribution used in generating cross sections for OH in LTE. Retrieved from 50 simulated secondary eclipses.

Table 2
Populations Corresponding to v States for the Normal Distribution (Non-LTE) Example and the Boltzmann LTE Example for Both Populations Arising from the Spin Splitting

v	Normal Population	Boltzmann Population Spin 1	Boltzmann Population Spin 2
0	0.0044	1.0000	0.9086
1	0.0540	0.1614	0.1467
2	0.2420	0.0283	0.0258
3	0.3990	0.0054	0.0049
4	0.2420	0.0011	0.0010
5	0.0540	…	…
6	0.0044	…	…

Previous studies (e.g., Brogi & Line 2019; Gibson et al. 2022) show that removing the telluric lines using a detrending method (e.g., airmass detrending, singular value decomposition, or SysRem) alters the planetary spectrum in the data. As cross-correlation or likelihood mapping is basically a template matching if the model is processed differently than the observed data, any constraint that relies on the line profile (strength, position, width, and shape) would be unreliable. To correct this effect, for each spectral order of each data set, we Doppler-shifted the model template for a given value of K_P and v_{sys} as a function of orbital phase and divided out the mean spectrum to normalize it. We then applied the preprocessing technique described by Gibson et al. (2022) that uses the same SysRem basis vectors that were used to remove the telluric lines and subtracted them out from the normalized Doppler-shifted model array. This preprocessed model array was then directly used to calculate the likelihood value. We repeated this process for a range of K_P and v_{sys}. To account for the different scaling of the model to the data, we calculated the likelihood for a range of α values. Last, previous literature (e.g., Gibson et al. 2020, 2022; Nugroho et al. 2020) estimated the significance of the detection by dividing the median values of the conditional distribution of α at the best-fit parameters by its standard deviation. Here, we expanded it to produce a significance map by performing it to all of the combinations of K_P and v_{sys}.

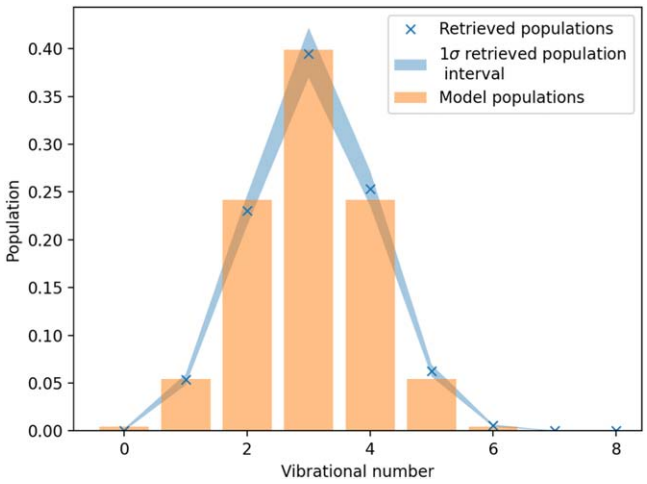

Figure 15. Retrieved mixing ratios for OH compared with simulated spectra generated using OH with a disequilibrium, normal distribution peaking at $v = 3$.

5.3. LTE Forward Model—All Bands

Using our OH LTE forward model, we obtained a strong detection of OH emission with an S/N of 9.5 at the K_P of 231.8 km s^{-1} and v_{sys} of -1.1 km s^{-1}, consistent with the previous detection (Figure 16(a)). With the preprocessed model and likelihood mapping, the same signal is detected at $>12\sigma$ (Figure 16(b)), demonstrating the advantage of the likelihood framework and preprocessing the model over a pure cross-correlation, without preprocessing the model in detecting atmospheric signal.

5.4. Individual Bands

Here, we tried to detect the individual OH band assuming a completely populated state for each band, similar to Figure 3. Rotational state populations are taken to be Boltzmann-distributed, while the vibrational state populations are unweighted in order to explore any non-LTE (non-Boltzmann) circumstances. For the high-resolution case, we extended our isolated cross-section setup to $v = 9$ (which corresponds to a maximum highest state of $v = 12$ via the $\Delta v = 3$ band) in order to reflect the potential for higher sensitivity than the lower-resolution modeling. We obtained a strong detection both for bands 0 and 1 at $>6\sigma$, consistent with the velocity of the planet detected using the OH LTE model. Unfortunately, there is no clear evidence for hotter vibrational bands, although there is a

Table 3
Summary of IRD Observations

Name of the Night	Date (UT)	Observing Time (UT)	Airmass Change	Phase Coverage	Number of Frames	Mean S/N (at 1 μm)	# SysRem Iterations
N1	2020-10-01	10:35-13:42	1.12-1.05-1.12	0.597-0.700	33	145	3
N2	2021-08-30	10:25-15:15	1.64-1.05-1.08	0.569-0.734	56	156	9
N3	2021-12-18	05:24-10:18	1.13-1.05-1.44	0.573-0.740	55	110	6

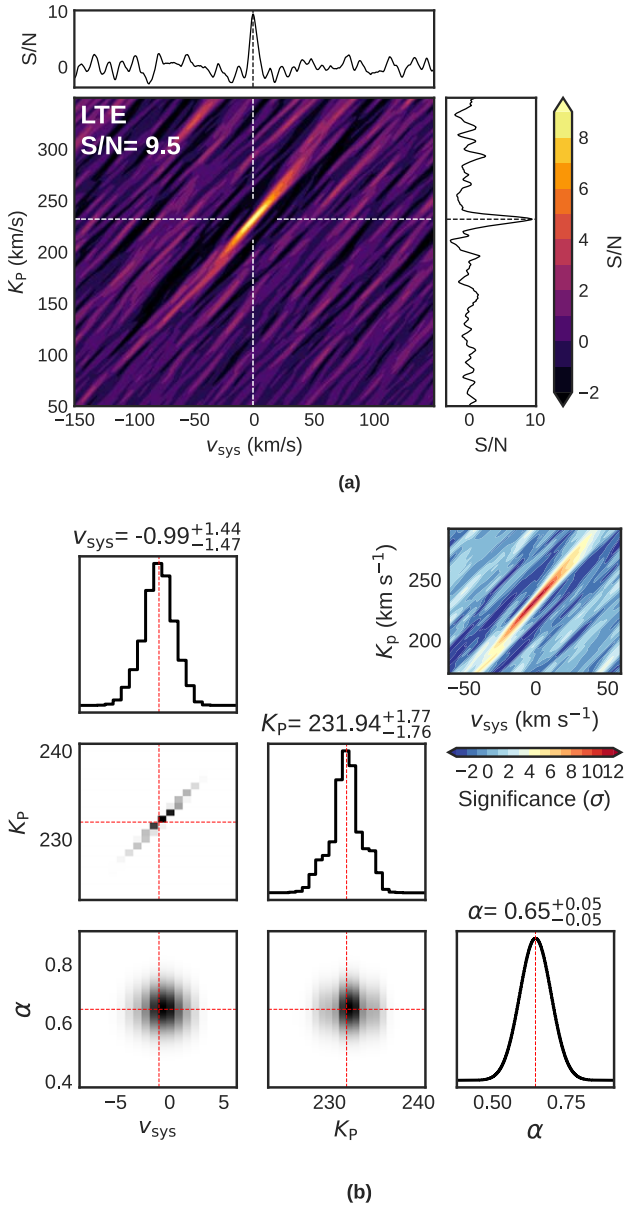

Figure 16. (a) The K_P–v_{sys} map after combining the cross-correlation functions of all of the data sets using a non-preprocessed OH LTE model. The upper panel shows the S/N curve at the K_P of 231.8 km s^{-1}, while the right panel shows the S/N curve at the v_{sys} of -1.1 km s^{-1}. The color bar shows the S/N of the K_P–v_{sys} map. (b) The marginalized likelihood distribution of K_P, v_{sys}, and α using a preprocessed OH LTE model. The red dashed lines show the median value of the corresponding distribution. The upper right panel is the K_P–v_{sys} map of the detection from the likelihood. The color bar shows the significance of the K_P–v_{sys} map. This map is produced by dividing the median value of the conditional likelihood distribution of α by its uncertainty at every combination of K_P and v_{sys}.

hint of a weak signal of band 2 in the K_P–v_{sys} significance map (see Figure 17(a)).

5.5. Band Unpeeling

High-resolution spectroscopy, obtained from ground-based instruments, contains a substantial noise component, due to sources such as the telluric lines from the Earth's atmosphere; in comparison, the component from the actual exoplanet's atmosphere has a low S/N. With this limitation, and since the individual bands in isolation provide even smaller signal contributions, we obtain inconclusive results when performing the cross-correlation technique with templates containing isolated vibrational bands.

To mitigate the limited contributions from individual bands, we attempt a spectral "unpeeling" approach; cross-correlation templates were constructed with bands sequentially added from 0 to 9 (i.e., bands 0, 0+1, 0+1+2, 0+1+2+3, etc.) and also backward from 9 to 0 (i.e., bands 9, 9+8, 9+8+7, …, 9+8+7 +6+5+4+3+2+1+0). We propose the unpeeling approach to include contributions from a greater number of bands in the model templates. This is to present an approach that may enhance the cross-correlation signal in circumstances where the individual band signals are too weak, while still performing some band isolation across sequential models, as is the goal of this technique. The combination of a number of the vibrational bands then yielded a recognizable change in the detection significance when comparing cross-correlation results between different templates (see Figures 17(b) and (c)). This change is especially significant from 0 to $0+1$, consistent with the 0 and 1 states being mainly populated at this temperature (see Section 5.4 and Figure 17(a)), and the high detection significance of the backward unpeeling model $9+8+7+6+5+4+3+2+1$ (i.e., with band 0 excluded). Meanwhile, the $9+8+7+6+5+4+3+2$ backward model (with bands 0 and 1 excluded) does not yield any detection, although visually we can see a possible signal of this model around the expected velocity of the planet, similar to the individual band 2 model in Section 5.4. This is also supported by the increase of the detection significance when band 2 is added into the $0+1$ band model. Interestingly, the single band 0 of the unpeeling band model yields a much stronger detection (9σ) than the completely populated (unity-scaled) $v0$ case (6.6σ). This difference in the detection significances arises from a difference in the model templates, driven by differing line intensities. These line intensities are governed by the vibrational state populations, which in the case of the completely populated model have been artificially set to unity, while in the filtered case the populations obey a Boltzmann distribution, but with filtering applied afterward to select the $v0$ model.

The difficulty of detecting vibrational hot bands is in principle in accordance with the LTE conditions corresponding

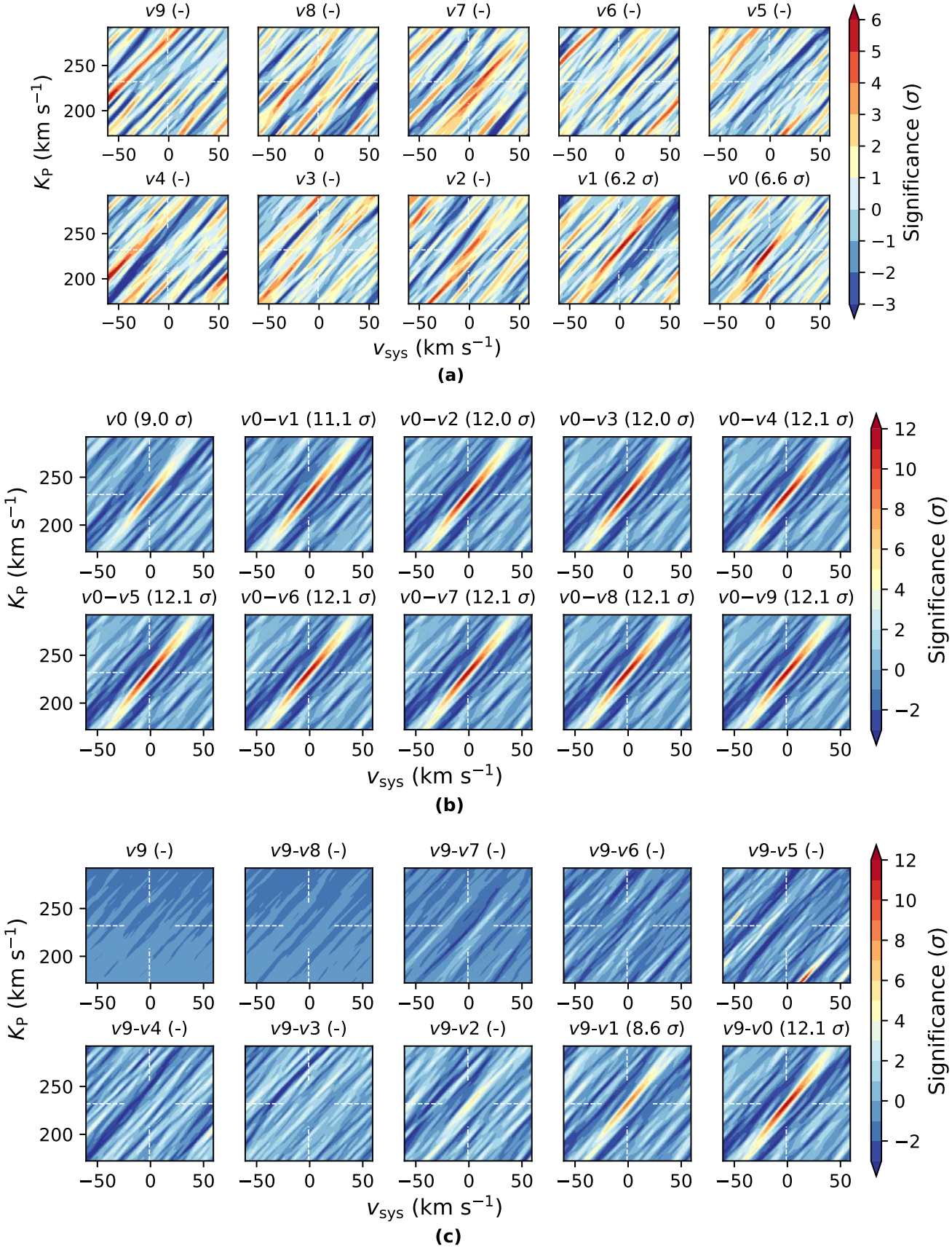

Figure 17. The K_P–v_{sys} significance map of the combined data sets ($N_1 + N_2 + N_3$) for the preprocessed individual band model (a), the unpeeling model from band 0 only to the total $0 + 1 + 2 + 3 + 4 + 5 + 6 + 7 + 8 + 9$ bands (b), and the unpeeling model from band 9 only to the sum of bands 0, 1, 2, 3, 4, 5, 6, 7, 8, and 9 (c). The white dashed lines indicate the location of the OH LTE model signal as a reference. The color bar shows the significance of the maps.

to the T-P profile temperature; the vibrational state populations relate to the detection significances for each individual band model, with only the first two detected in line with Boltzmann-distributed populations corresponding to a vibrational temperature consistent with the effective temperature. This difficulty of detection is also related to the limited NIR region used, which does not properly cover the contributions of the hot bands $v'' > 5$.

6. Discussion

Although the wavelength separation is good for the individual hot bands of molecules such as OH, the ability to distinguish between the bands in all situations is not unlimited and sufficient wavelength range coverage is required to avoid degeneracy. This limitation becomes apparent when attempting retrievals on spectra for state populations peaking at higher vibrational numbers. For instance, using the current wavelength coverage of 0.97–1.5 μm in atmospheric retrievals, it would be difficult to detect the terrestrial-like airglow population, which is known to peak at the higher vibrational band (8, 6) (Chen et al. 2021). When attempting a retrieval of this non-LTE scenario, we encountered a substantial overestimation of the corresponding vibrational band—(7, 5) or (8, 6)—abundances, characterized by a convergence to the top boundary of the prior when fitting via a nested sampling method. This problem exists for these higher bands when observing over this wavelength range, since the stronger band becomes truncated; to constrain these bands, a wavelength coverage reaching higher wavelengths would be required.

As the ground-truth population for a given state becomes small, the associated transition lines in the spectrum become weaker. When this weakness becomes sufficiently small compared to the observation uncertainty (simulated, in this case), the populations for these states are no longer retrievable. This can be seen in Figure 14, where it is characterized by a far wider 1σ interval for the retrieved $v = 4$ population.

It is theoretically possible to add an additional level of complexity and also attempt retrieval of fine-structure spin-splitting state populations, for which theoretical values are represented by the overlapping bars for each vibrational number in Figure 14. OH in this electronic configuration is characterized by spin splitting of 126.3 cm^{-1}. The quantum number assignments available in this line list are sufficient to do this theoretically, but since the observational data quality is limited, we leave this for future work.

WASP-33 is a pulsating δ-Scuti variable (Changeat et al. 2022), which makes it a slightly more complex system; this should not be an issue for the high-resolution analysis, as there is no OH in the stellar atmosphere to affect the cross-correlation results.

Possible further work could explore using this technique for a range of other molecules (such as TiO or other diatomics, due to their good vibrational band separation) and a range of other data sets, including different wavelength ranges and target planets. One such candidate could be WASP-18b, where OH has also been detected (Brogi et al. 2023).

7. Conclusion

From the analysis conducted here, we can conclude that individual vibrational state populations can be obtained for OH in NIR as fitted parameters in exoplanet atmosphere retrieval techniques by including isolated individual bands as cross sections of individual species. Here, we have shown the viability of this approach for OH, though this generalizes to diatomic molecules more broadly on account of their good vibrational band separation. Not only is this shown for simulated observational spectra for OH with a typical LTE Boltzmann distribution across vibrational states, but also for a nonequilibrium case. In addition, we demonstrate that non-Boltzmann distributions are also retrievable: for the nonequilibrium case, this approach can also distinguish where higher states are populated, as in the example of the $v = 3$ peak normal population model. The detection of such a higher peak, or retrieved populations incongruous with the Boltzmann distribution, in observed data would be consistent with a non-LTE signature.

To facilitate the individual vibrational band detection, an "unpeeling" model is suggested, where individual band contributions are added to or subtracted from the total cross sections. Applying an unpeeling approach to the recent high-resolution detection of individual bands of OH in WASP-33b, we obtained a significant difference when band 1 was added to a single band 0 model, illustrating the potential of detection of individual spectroscopic bands.

Acknowledgments

This research is based (in part) on data collected at the Subaru Telescope, which is operated by the National Astronomical Observatory of Japan. We are honored and grateful for the opportunity of observing the Universe from Maunakea, which has cultural, historical, and natural significance in Hawaii. Our data reductions benefited from PyRAF and PyFITS, which are products of the Space Telescope Science Institute, which is operated by AURA for NASA. We are also grateful to the developers of the NUMPY, SCIPY, MATPLOTLIB, JUPYTER NOTEBOOK, and ASTROPY packages, which were used extensively in this work (Hunter 2007; Astropy Collaboration et al. 2013; Kluyver et al. 2016; Price-Whelan et al. 2018; Virtanen et al. 2020). Funding: S.W. was supported by the STFC UCL Centre for Doctoral Training in Data Intensive Science (grant number ST/P006736/1). This project received funding from the European Research Council (ERC) under the European Union's Horizon 2020 research and innovation program (grant agreements 758892, ExoAI and 883830, ExoMolHD) and the European Union's Horizon 2020 COMPET program (grant agreement No. 776403, ExoplANETS A). Furthermore, we acknowledge funding by UK Space Agency and Science and Technology Funding Council (STFC) grants: ST/R000476/1, ST/K502406/1, ST/P000282/1, ST/P002153/1, ST/S002634/1, and ST/T001836/1. The authors acknowledge the use of the UCL Legion High Performance Computing Facility (Legion@UCL) and associated support services in the completion of this work, along with the Cambridge Service for Data Driven Discovery (CSD3), part of which is operated by University of Cambridge Research Computing on behalf of the STFC DiRAC HPC Facility (www.dirac.ac.uk). The DiRAC component of CSD3 was funded by BEIS capital funding via STFC capital grants ST/P002307/1 and ST/R002452/1 and STFC operations grant ST/R00689X/1. DiRAC is part of the National e-Infrastructure. This work was supported by JSPS KAKENHI grant Nos. JP22K14092, JP19K14783, JP21H00035, JP20H00170, 21H04998, and SATELLITE Research from the Astrobiology center (AB022006). J.L.B. acknowledges funding from the European

Research Council (ERC) under the European Union's Horizon 2020 research and innovation program, under grant agreement No. 805445.

Data Availability

The underlying molecular line list data from the ExoMol project (Tennyson et al. 2020) are available from the Exomol website (www.exomol.com). Derived cross-section data are available from the corresponding author upon request.

ORCID iDs

Sam O. M. Wright https://orcid.org/0000-0002-3852-9562
Stevanus K. Nugroho https://orcid.org/0000-0003-4698-6285
Matteo Brogi https://orcid.org/0000-0002-7704-0153
Neale P. Gibson https://orcid.org/0000-0002-9308-2353
Ernst J. W. de Mooij https://orcid.org/0000-0001-6391-9266
Ingo Waldmann https://orcid.org/0000-0002-4205-5267
Jonathan Tennyson https://orcid.org/0000-0002-4994-5238
Hajime Kawahara https://orcid.org/0000-0003-3309-9134
Masayuki Kuzuhara https://orcid.org/0000-0002-4677-9182
Teruyuki Hirano https://orcid.org/0000-0003-3618-7535
Takayuki Kotani https://orcid.org/0000-0001-6181-3142
Yui Kawashima https://orcid.org/0000-0003-3800-7518
Kento Masuda https://orcid.org/0000-0003-1298-9699
Jayne L. Birkby https://orcid.org/0000-0002-4125-0140
Chris A. Watson https://orcid.org/0000-0002-9718-3266
Motohide Tamura https://orcid.org/0000-0002-6510-0681
Konstanze Zwintz https://orcid.org/0000-0001-9229-8315
Hiroki Harakawa https://orcid.org/0000-0002-7972-0216
Tomoyuki Kudo https://orcid.org/0000-0002-9294-1793
Klaus Hodapp https://orcid.org/0000-0003-0786-2140
Shane Jacobson https://orcid.org/0000-0003-1438-4124
Mihoko Konishi https://orcid.org/0000-0003-0114-0542
Jun Nishikawa https://orcid.org/0000-0001-9326-8134
Masashi Omiya https://orcid.org/0000-0002-5051-6027
Sébastien Vievard https://orcid.org/0000-0003-4018-2569
Sergei N. Yurchenko https://orcid.org/0000-0001-9286-9501

References

Al-Refaie, A. F., Changeat, Q., Waldmann, I. P., & Tinetti, G. 2021, ApJ, 917, 37
Astropy Collaboration, Robitaille, T. P., Tollerud, E. J., et al. 2013, A&A, 558, A33
Birkby, J. L., de Kok, R. J., Brogi, M., et al. 2013, MNRAS, 436, L35
Borsa, F., Fossati, L., Koskinen, T., Young, M. E., & Shulyak, D. 2021, NatAs, 6, 226
Brogi, M., Emeka-Okafor, V., Line, M. R., et al. 2023, AJ, 165, 91
Brogi, M., & Line, M. R. 2019, ApJ, 157, 114
Brooke, J. S. A., Bernath, P. F., Western, C. M., et al. 2016, JQSRT, 138, 142
Changeat, Q., Edwards, B., Al-Refaie, A. F., et al. 2022, ApJS, 260, 3
Chen, Q., Hu, X., Guo, H., & Xie, D. 2021, J. Phys. Chem. Lett., 12, 1822
Clancy, R. T., Sandor, B. J., Garcia-Munoz, A., et al. 2013, Icar, 226, 272
Clark, V. H. J., & Yurchenko, S. N. 2021, PCCP, 23, 11990
Cont, D., Yan, F., Reiners, A., et al. 2021, A&A, 651, A33
Cont, D., Yan, F., Reiners, A., et al. 2022, A&A, 657, L2
Edwards, B., & Stotesbury, I. 2021, AJ, 161, 266
Fisher, C., & Heng, K. 2019, ApJ, 881, 25
Fossati, L., Young, M. E., Shulyak, D., et al. 2021, A&A, 653, A52
Gibson, N. P., Merritt, S., Nugroho, S. K., et al. 2020, MNRAS, 493, 2215
Gibson, N. P., Nugroho, S. K., Lothringer, J., Maguire, C., & Sing, D. K. 2022, MNRAS, 512, 4618
Guillot, T. 2010, A&A, 520, A27
Han, S., Zhao, B., Conte, R., et al. 2022, JPCA, 126, 6944
Hunter, J. D. 2007, CSE, 9, 90
Kluyver, T., Ragan-Kelley, B., Pérez, F., et al. 2016, in Positioning and Power in Academic Publishing: Players, Agents and Agendas, ed. F. Loizides & B. Schmidt (Amsterdam: IOS Press), 87
Kotani, T., Tamura, M., Nishikawa, J, et al. 2018, Proc. SPIE, 10702, 1070211
Kuzuhara, M., Hirano, T., Kotani, T., et al. 2018, Proc. SPIE, 10702, 1070260
Meinel, I. A. B. 1950, ApJ, 111, 555
Merritt, S. R., Gibson, N. P., Nugroho, S. K., et al. 2020, A&A, 636, A117
Noll, S., Winkler, H., Goussev, O., & Proxauf, B. 2020, ACP, 20, 5269
Nugroho, S. K., Gibson, N. P., de Mooij, E. J. W., et al. 2020, ApJL, 898, L31
Nugroho, S. K., Kawahara, H., Gibson, N. P., et al. 2021a, ApJL, 910, L9
Nugroho, S. K., Kawahara, H., Gibson, N. P., et al. 2021b, ApJL, 910, L9
Nugroho, S. K., Kawahara, H., Masuda, K., et al. 2017, AJ, 154, 221
Öberg, K. I., Murray-Clay, R., & Bergin, E. A. 2011, ApJL, 743, L16
Oliva, E., Origlia, L., Scuderi, S., et al. 2015, A&A, 581, A47
Pastorek, A., Clark, V. H., Yurchenko, S. N., Ferus, M., & Civiš, S. 2022, Spectra Chimica Acta A, 278, 121322
Pontoppidan, K. M., Pickering, T. E., Laidler, V. G., et al. 2016, Proc. SPIE, 9910, 381
Price-Whelan, A. M., Sipőcz, B. M., Günther, H. M., et al. 2018, AJ, 156, 123
Rousselot, P., Lidman, C., Cuby, J. G., Moreels, G., & Monnet, G. 2000, A&A, 354, 1134
Snellen, I. A. G., de Kok, R. J., de Mooij, E. J. W., & Albrecht, S. 2010, Natur, 465, 1049
Tamura, M., Suto, H., Nishikawa, J., et al. 2012, Proc. SPIE, 8446, 84461T
Tamuz, O., Mazeh, T., & Zucker, S. 2005, MNRAS, 356, 1466
Tennyson, J., Yurchenko, S. N., Al-Refaie, A. F., et al. 2020, JQSRT, 255, 107228
Tessenyi, M., Tinetti, G., Savini, G., & Pascale, E. 2013, Icar, 226, 1654
Treanor, C. E., Rich, J. W., & Rehm, R. G. 1968, JChPh, 48, 1798
van Sluijs, L., Birkby, J. L., Lothringer, J., et al. 2023, MNRAS, 522, 2145
Virtanen, P., Gommers, R., Oliphant, T. E., et al. 2020, NatMe, 17, 261
Wright, S. O. M., Waldmann, I., & Yurchenko, S. N. 2022, MNRAS, 512, 2911
Yan, F., Pallé, E., Reiners, A., et al. 2022, A&A, 661, L6
Yan, F., Wyttenbach, A., Casasayas-Barris, N., et al. 2021, A&A, 645, A22
Yurchenko, S. N., Al-Refaie, A. F., & Tennyson, J. 2018, A&A, 614, A131